Atmos. Meas. Tech. Discuss., 8, 11925–11952, 2015
www.atmos-meas-tech-discuss.net/8/11925/2015/
doi:10.5194/amtd-8-11925-2015

Atmospheric Measurement Techniques Discussions

Observations of water vapor mixing ratio and flux in Tibetan Plateau

S. Wu[1], G. Dai[1], X. Song[1], B. Liu[1], and L. Liu[2]

[1]Ocean Remote Sensing Institute, Ocean University of China, Qingdao, China
[2]Laboratory of Severe Weather, Chinese Academy of Meteorological Science, Beijing, China

Received: 7 October 2015 – Accepted: 26 October 2015 – Published: 16 November 2015

Correspondence to: S. Wu (wush@ouc.edu.cn)

Published by Copernicus Publications on behalf of the European Geosciences Union.

Abstract

The water vapor expedition experiment campaign was operated in the Tibetan Plateau during July and August 2014, by utilizing the Water vapor, Cloud and Aerosol Lidar (WACAL). The observation was carried out in Nagqu area (31.5° N, 92.05° E), which is 4508 m above the mean sea level. During the observation, the water vapor mixing ratio at high elevation was obtained. In this paper, the methodology of the WACAL and the retrieval method are presented in particular. The validation of water vapor mixing ratio measured during the field campaigns is completed by comparing the Lidar measurements to the radiosonde data. WACAL observations from July to August illustrate the diurnal variation of water vapor mixing ratio in the planetary boundary layer in this high elevation area. The mean water vapor mixing ratio in Nagqu in July and August is about 9.4 g kg^{-1} and the values vary from 6.0 to 11.7 g kg^{-1} near ground. The SNRs and relative errors of the data are analyzed and discussed as well in this paper. Finally, combining the vertical wind speed profiles measured by the coherent wind lidar, the vertical flux of water vapor is calculated and the upwelling and deposition of the water vapor are monitored. It is the first application, to our knowledge, to operate continuously atmospheric observation by utilizing multi-disciplinary lidar at altitude higher than 4000 m which is significant for research on the boundary dynamics and meteorology of Tibetan Plateau.

1 Introduction

Although the content of water vapor in the atmosphere is very rare and occupies about 0.1–3 % of the content of the atmosphere, water vapor has a significant impact on the determination of weather and climate due to the fundamental role in the radiative energy transfer, hydrological cycle, and atmospheric chemistry processes. Through coupling with clouds, water vapor influences the radiative budget of earth both directly and indirectly. Moreover, because of its strong absorption and emission bands, especially in

AMTD
8, 11925–11952, 2015

the infrared, water vapor is one of the most significant greenhouse gas. Slight change in the water vapor profile might brings pronounced affect on the global warming process. It also influences atmospheric circulation and temperature structure by condensation and evaporation processes (Dinoev, 2009). Aiming at the detection of water vapor, the most commonly used method is radiosonde. The humidity sensors in radiosonde, which detect changes in resistance or dielectric constant resulting from absorption or adsorption of water (Wang et al., 2003), are installed. Several inter-comparison studies (Ferrare et al., 1995; Turner and Goldsmith, 1999) have been operated to test the stability of these sensors. As a result, strong systematic differences between different sensors are present for all ranges of humidity and temperature. Consequently, requirement for the new techniques seem to be very significant. Lidar, as an active remote sensing technique, has the advantage of high temporal and spatial resolution, high-frequency dynamic monitoring. Two Lidar (LIght Detect And Ranging) techniques have been applied to the detection of water vapor: the Differential Absorption Lidar (DIAL) and the Raman Lidar technique. In terms of the DIAL, two laser pulses at different wavelengths, called "on-line" and "off-line", respectively, are emitted to the atmosphere (Browell, 1983; Grant, 1991; Wulfmeyer and Bösenberg, 1998; Bruneau et al., 2001). In this paper, the Lidar system applies Raman technique. This technique was firstly used by Melfi (1969, 1972) and Cooney (1970) and the profiles of water vapor mixing ratio were retrieved and provided. The Raman Lidar technique depends on the detection of Raman backscattered radiation from atmospheric molecules (Melfi et al., 1969, 1972; Renaut and Capitini, 1988). The process of Raman scattering is characterized by a wavelength shift of the scattered radiation in respect to the exciting wavelength. The shift is uniquely associated with the internal transitions between the rotational-vibrational energy levels of the molecules (Inaba, 1976; Demtroder, 2005), and is used for identification of the scattering molecules. Due to the development of the high power laser source, the vertical operation range of the Raman Lidars can be extended up to 7 km (Whiteman et al., 1992) and throughout the troposphere (Vaughan et al., 1988; Goldsmith, 1998).

AMTD
8, 11925–11952, 2015

The Tibetan Plateau lies at a critical and sensitive junction of four climatic systems: the Westerlies, the East Asian Monsoon, the Siberian cold polar airflow and the Indian monsoon. In turn, the Tibetan Plateau influences the atmosphere in East Asia area and even the whole Northern Hemisphere. The Tibetan Plateau has great impact on the water vapor budget of area around. The water vapor transportation based on the plateau-monsoon interaction affects the drought and flood of Asia and even the whole north hemisphere. Consequently, it is a significant scientific problem to study the development of water vapor in Tibetan Plateau. During the 2014 Tibetan Plateau atmospheric expedition experiment campaign, the vertical profiles of water vapor mixing ratio are measured by WACAL.

2 Methodology

During the routine observation from 10 July to 16 August, the water vapor mixing ratio is monitored twice one day (00:00 and 12:00 UTC) by the applying of operational radiosondes. However, because of the limitation of the temporal resolution and measurement frequency, the water vapor mixing ratio data from radiosonde cannot satisfy the requirement of nowcast due to the various meteorological situation, especially in the high elevation area with strong radiation and convection. With the development of the knowledge, some other remote sensing techniques appear. These techniques include passive and active remote sensing. The paper introduces the Lidar, an active sensing technique. The Lidar is capable of providing vertical water vapor mixing ratio with the advantages of high temporal and spatial resolution.

The principle and basic layout of WACAL is described in this section for the integrality and the detailed design is described in a separated paper. Figure 1 shows the schematic diagram of WACAL.

The laser at wavelengths of 354.7, 532 and 1064 nm are transmitted to the atmosphere after the beam expanders. The diameter of laser at wavelength of 354.7 nm is expended from 9 mm to 9 cm and the divergence angle of the beam is reduced to

AMTD
8, 11925–11952, 2015

0.05 mrad. After scattered by the molecular and particles, the backscatter signal is collected by a four-telescope assembly.

Here the rotational-vibrational Raman spectrum of nitrogen and water vapor are explained. According to the selection rule for vibrational transitions, the change of the vibrational quantum number $\Delta\upsilon = 0, \pm 1, \pm 2, \ldots$. However, when come to the area of atomic fine structure and atomic physics, the sublevels cannot be ignored. And the change of the rotational quantum number ΔJ obeys to the transition selection rule $\Delta J = 0, \pm 2$. In turn, the $\Delta\upsilon$ and ΔJ can describe the transitions of the atoms. So because of the presence of sublevels, several branches of rotational-vibrational Raman spectrum can be detected as Table 1 shows.

In this paper, the Q-branch ($\Delta\upsilon = 1, \Delta J = 0$) is applied for the detection. The shift of wave number Δk of nitrogen and water vapor are listed in Table 2.

Since the Raman scattering signal is 2 to 3 orders of magnitude weaker than Rayleigh scattering signal, the detection of the Raman signal at wavelength of 386.7 and 407.5 nm is more difficult due to the much lower SNR. The backscattered laser light is collected by four 304.8 mm in diameter telescopes with focal length of 1524 mm. For the better receiving efficiency and lower height to fit in the compact container, these four telescopes are assembled as a telescope array, and the efficient aperture of receiver widens to 609.6 mm. Four fibers are mounted at the focus of the telescopes for the coupling of the signal. The core of the fibers is 200 microns and the numerical aperture is 0.22, which also serves as a field stop. After the coupling of fiber, the Raman signal is delivered to the spectrophotometer and separated as nitrogen Raman signal and water vapor Raman signal. Meanwhile, the 532 and 1064 nm Mie and Rayleigh signal are transmitted to the polarization channel and the infrared channel respectively. With the help of the polarization channel, the measurements of depolarization ratio, extinction coefficient and clouds are solved, which are not described in details in this paper.

The Raman channel is shown in Fig. 1c. In this figure, the transmitter, receiver and spectrophotometer are provided in details. For purpose of avoiding the interference of

AMTD
8, 11925–11952, 2015

the elastic backscatter signal, band-pass filters are used. The center wavelength of the filters is 390 nm and the FWHM is 44.6 nm. The transmission between 370 and 410 nm is bigger than 93 % and the OD is bigger than 5 for light at the wavelength of 354.7 and 532 nm. After the filters, four fibers are mounted for the coupling of the signal. After the coupling of fiber, the Raman signal is delivered to the spectrophotometer and separated as Raman signal of nitrogen and water vapor.

When the signal is transmitted to spectrophotometer, the light is dispersed and then collimated by the convex lens with the focal length of 50.0 mm. After the reflection of the reflecting prism, the parallel light arrives at the grating. The groove density of the grating is 1302 L mm^{-1} and the blaze is 400 nm. So far, the Raman signal of nitrogen and water vapor are separated. Then the filters are used to ensure the purity of each signal at 386.7 and 407.5 nm. The center wavelength (CWL) of the filter-1 is 407.5 ± 0.1 nm. Meanwhile, the CWLs are 386.7 ± 0.1 nm and 354.7 ± 0.08 nm for filter-2 and filter-3, respectively. The FWHM of all filters is 0.5 ± 0.10 nm and peak transmittance is bigger than 50 % and OD is 5 when out of band blocking from 200 to 1200 nm. After the filtration of filters, the parallel signal is then focused by plano-convex lens with a focal length of 100 mm. Finally, the signals are acquired by the photomultiplier tubes which are mounted at the focal point of plano-convex lens. The specifications of the optical elements of this channel are shown in Table 3.

The Lidar equation can be described as

$$P(z,\lambda_R) - P_{BG} = P_0(\lambda_L)\Delta z \frac{A_0 O(z)}{z^2}\xi(\lambda_R)\beta_R^{\pi}(z,\lambda_R)T^{up}(z,\lambda_L)T^{down}(z,\lambda_R) \quad (1)$$

$$T^{up}(z,\lambda_L) = \exp\left[-\int_{z_0}^{z}\alpha(z',\lambda_L)\mathrm{d}z'\right]$$

$$T^{down}(z,\lambda_R) = \exp\left[-\int_{z}^{z_0}\alpha(z',\lambda_R)\mathrm{d}z'\right] \quad (2)$$

AMTD
8, 11925–11952, 2015

where $P_0(\lambda_L)$ is the laser pulse energy, Δz is the range resolution, A_0 is the aperture of the telescope, $\xi(\lambda_R)$ is the receiving efficiency at a given wavelength, $\beta_R^{\pi}(z,\lambda_R)$ is the backscatter coefficient at λ_R, $\alpha(z,\lambda_L)$ is the extinction coefficient, $T^{up}(z,\lambda_L)$ and $T^{down}(z,\lambda_R)$ are the atmospheric transmission at λ_L and λ_R respectively.

According to Eq. (1), the backscatter signal of N_2 and H_2O are obtained as $P(z,\lambda_{N_2})$ and $P(z,\lambda_{H_2O})$. The water vapor mixing ratio can be calculated by Eq. (3):

$$w(z) = C\frac{P(z,\lambda_{H_2O})}{P(z,\lambda_{N_2})}\Delta T(\lambda_{N_2},\lambda_{H_2O},z) \tag{3}$$

where: C is calibration constant and can be obtained by contrast of Lidar data and radiosonde data, $\Delta T(\lambda_{N_2},\lambda_{H_2O},z)$ is the differential atmospheric transmission at nitrogen and water vapor Raman wavelengths and is calculated by Eq. (4):

$$\Delta T(\lambda_{N_2},\lambda_{H_2O},z) = \exp\left(-\int_{z_0}^{z}\left[\alpha(z',\lambda_{N_2}) - \alpha(z',\lambda_{H_2O})\right]\mathrm{d}z'\right) \tag{4}$$

The calibration constant is retrieved using regression to a vertical water vapor mixing ratio profile obtained by a reference radiosonde. The radiosonde provides temperature profiles with measurement accuracy of 2 %. Additionally the pressure and relative humidity profiles are also obtained. The Eq. (5) is used to obtain a mixing ratio profile from radiosonde data. In this equation, the temperature, pressure and relative humidity profiles are used and the mixing ratio WR ($g\,kg^{-1}$) is then estimated.

$$\mathrm{WR} = \varphi \times \frac{0.622 \times P_s(T)}{P - 0.378 \times P_s(T)} \tag{5}$$

where: φ is relative humidity, P is the pressure and P_s is the saturated vapor pressure at temperature T and can be calculated by Eq. (6):

$$P_s(T) = 6.1121 \times \exp\left(\left(18.678 - \frac{T}{234.5}\right) \times \left(\frac{T}{257.14 + T}\right)\right) \tag{6}$$

AMTD
8, 11925–11952, 2015

The calibration constant for this comparison was obtained by regressing the lidar profile (up to 5 km) to radiosonde as shown in Fig. 2. The lidar water vapor mixing ratio (W_{Lidar}) profile was calculated according to Eq. (3) with a calibration constant set to one. We assume that the relationship between Lidar data $W_{\text{Lidar}} = \Delta T(\lambda_{N_2}, \lambda_{H_2O}, z) \times P(z, \lambda_{H_2O})/P(z, \lambda_{N_2})$ and radiosonde data W_{Sonde} as Eq. (7):

$$W_{\text{Sonde}} = C \times W_{\text{Lidar}} + D \tag{7}$$

Before the field campaign in the Tibetan Plateau, the water vapor profiles of WACAL were compared with the radiosonde at the campus of Ocean University of China in Qingdao. Since the radiosondes were launched every day at 00:00 and 12:00 UTC, the Lidar measurements covered the period for the purpose of validation. The radiosondes were launched at the site of Meteorological Administration of Qingdao (36.07° N, 120.33° E) everyday, while the WACAL was deployed at Ocean University of China (36.165° N, 120.4956° E). As Fig. 2a shows, the distance between these two sites is 16.7 km. In Table 4, the period of time of the simultaneous observations by radiosonde and WACAL is provided.

Using the linear model, the lidar and radiosonde profiles are fitted. The slope C from the fit is a direct estimation of the lidar calibration constant, and is found to be equal to 219. Meanwhile, the D is determined as 0.34. As Fig. 2 shows, the correlation coefficient of these two system data can reach up to 0.83. The standard deviation is 1.4 and the number of samples is 169. After the calibration the water vapor mixing ratio can be rewritten as Eq. (8):

$$W_{\text{Lidar}}^{\text{Cal}} = 219 \times W_{\text{Lidar}} - 0.34 \tag{8}$$

3 Observation consequences and discussion

Atmospheric observations were operated in Tibetan Plateau during 10 July and 16 August 2014 by utilizing the WACAL. The Tibetan Plateau atmospheric expedition exper-

AMTD
8, 11925–11952, 2015

iment campaign had been carried out in Nagqu (31.5° N, 92.05° E), which is 4508 m above the mean sea level.

In our system, both of AD (Analog-to-Digital) signal and PC (Photon Counting) signal are detected by the photomultiplier tube (PMT). However, Data acquisition by the PC method is possible only when the photons are individually distinguishable (Whiteman et al., 1992). In other words, because of the saturation effect and the bandwidth limitation of PMTs, the response of counting system is nonlinear. As a result, we have to correct Nitrogen and Oxygen echo signal by the equation next:

$$P_{\text{real}} = \frac{P_{\text{meas}}}{1 - \tau \times P_{\text{meas}}} \tag{9}$$

where P_{real} is the actual number of photons detected by PMTs, P_{meas} is the measured number and τ is the resolving time of the discriminator counter combination of PMTs, which is also known as dead-time. After the correction, the actual signal of nitrogen and water vapor Raman signal will be draw in Fig. 3.

Aiming at the validation of the calibration, the scatter diagram based on the calibrated Lidar data and radiosonde data measured in Nagqu is drawn as Fig. 4:

According to the figure above, the correlation coefficient can reach up to 93.54 % and mean deviation is 0.77 g kg^{-1}. As a conclusion, the calibration of the water vapor mixing ratio is accurate enough for the routine observation. Here we will provide some case studies in Fig. 5 for the discussion. Several inter-comparisons of Lidar derived vertical profiles with radiosondes are presented (Fig. 5) as well as time series of water vapor mixing ratio in Nagqu from 10 July to 16 August (Fig. 6).

In Fig. 5, the blue dashed line indicates the water vapor mixing ratio measured by Lidar and the pink line shows the error bar of the data. Meanwhile the red line shows the data which are gotten from the operational radiosonde. From these four figures, one dry layer could be seen at about 2.8 to 3 km in figure (a) and one distinct wet layer could be seen at about 1.5 to 2 km in figure (c). And in figure (b) and (d), the water

AMTD
8, 11925–11952, 2015

vapor mixing ratio gradually decrease as height increase. All of the water vapor mixing ratio profiles is averaged every 60 min and the range resolution is 75 m.

Note that Nagqu is located in inland area, the content of water vapor in Nagqu is abundant. It is likely that this phenomenon may result from the abundant vegetation, precipitation and strong evaporation from near plateau lakes in July and August. However, since the nitrogen concentration at altitude of 4508 m is about 42 % lower than at sea level altitude, the density and the backscatter coefficient of water vapor is also lower in Nagqu. Consequently, the measurement Signal-to-Noise-Ratio (SNR) is getting smaller and the error bar is bigger.

According to the profiles of water vapor mixing ratio, the observation data of the Lidar and operational radiosonde have a good consistency. However, the divergence cannot be ignored. Since the background light in Nagqu was still strong at 20:00 LST (LST = UTC + 8), it is difficult to measure the water vapor mixing ratio accurately by WACAL. For ensuring the accuracy of the measurement, WACAL was utilized from 21:30 LST, which is 1.5 h later than the measurement of radiosonde. The measuring time difference may be the main error source of observation in Nagqu.

Here the time serials of water vapor mixing ratio profile at 13:30 UTC from July, 10 to 16 August is shown in Fig. 6. The trend and variation of the water vapor during this summer field observation can be distinctly illustrated. According to Fig. 6a, the trend of $W_{\text{Lidar}}^{\text{Cal}}$ was getting smaller with the development of the time in July and August which might result from the gradually withered vegetation. In July, the vegetation is abundant in Nagqu. And maybe because of the transpiration of plants, water vapor content is rich. However, in August, the wilt of vegetation may lead to the decrease of water vapor content.

In the following section, the error of the signal and results are discussed. For the purpose of determining detection performance of the Lidar system, the SNR is taken into consideration. The SNR can be described as Eq. (8) (Papayannis et al., 1990;

AMTD
8, 11925–11952, 2015

Pelon and Mégie, 1982):

$$\mathrm{SNR}_i = \frac{P_i}{\sqrt{P_i + P_{\mathrm{bi}}}} \tag{10}$$

where P_i is backscatter signal, P_{bi} is the solar background signal.

Moreover, from Eq. (3), the relative error δ_{RE} can also be calculated by Eq. (9):

$$\delta_{\mathrm{RE}} = \frac{1}{\sqrt{N}} \left(\frac{1}{\mathrm{SNR}_1^2} + \frac{1}{\mathrm{SNR}_2^2} \right) \tag{11}$$

where N is the number of profiles used for average. SNR_1 and SNR_2 are the signal to noise ratio of nitrogen and water vapor respectively.

Here we will present one case study of the SNR and δ_{RE} in the following figure.

In Fig. 7, the SNR and relative error are analyzed. Because of the limitation of the lower water vapor content, the acceptable detection range is 3.5 km. The biggest SNR for nitrogen and water vapor in this observation are 6.8 and 0.22, respectively.

During the experiment campaign, for purpose of detection the flux of water vapor, the wind field is measured by utilizing a compact Coherent Doppler Lidar developed by the OUC lidar group. The Coherent Doppler lidar takes advantage of the fact that the frequency of the echo signal is shifted compared to the local-oscillator light because of the Doppler affect which occurs from backscattering of aerosols. The Doppler shift in the frequency of the backscattered signal is analyzed to calculate the line-of-sight (LOS) velocity component of the air motion. The Doppler shift f_{D} can be obtained by Eq. (10):

$$f_{\mathrm{D}} = \frac{2|\boldsymbol{V}_{\mathrm{LOS}}|}{\lambda} \tag{12}$$

where $\boldsymbol{V}_{\mathrm{LOS}}$ is the line-of-sight (LOS) velocity, λ is the laser wavelength and is equal to 1550 nm in this lidar system.

AMTD
8, 11925–11952, 2015

When the LOS velocities in four directions $\boldsymbol{V}_{\mathrm{LOS,E}}$, $\boldsymbol{V}_{\mathrm{LOS,W}}$,$\boldsymbol{V}_{\mathrm{LOS,S}}$ and $\boldsymbol{V}_{\mathrm{LOS,N}}$ are measured, the vertical wind speed can be calculated by Eq. (11) (Cariou, 2011):

$$\boldsymbol{V}_{\mathrm{ver}} = \frac{1}{4\sin\theta}(\boldsymbol{V}_{\mathrm{LOS,E}} + \boldsymbol{V}_{\mathrm{LOS,W}} + \boldsymbol{V}_{\mathrm{LOS,S}} + \boldsymbol{V}_{\mathrm{LOS,N}}) \quad (13)$$

where θ is the elevation angle.

With the synchronized observations of the water mixing ratio and vertical velocity, the vertical water vapor flux $\mathrm{Flux}_{\mathrm{WV,ver}}$ can be calculated by Eq. (12):

$$\mathrm{Flux}_{\mathrm{WV,ver}} = \rho_{\mathrm{WV}} \times |\boldsymbol{V}_{\mathrm{ver}}| \quad (14)$$

where ρ_{WV} is the absolute humidity that can be obtained from the water vapor mixing ratio.

In term of the vertical velocity and vertical water vapor flux, one case study on 15 August 2014 is presented below. Figure 8a is the time serials of the vertical velocity profile of 164 min obtained from the Coherent Doppler Wind Lidar. By combining absolute humidity (Fig. 8b) and vertical velocity data, the vertical water vapor flux can be calculated and the temporal development is shown in Fig. 9.

Vertical profiles in Fig. 8b indicates that the water vapor mixing ratio inside clouds is higher than in atmosphere around. From these figures, it is noted that the water vapor kept rising during 21:03 and 22:09 LST before the raining. Meanwhile in the process of raining, the water vapor inside the clouds kept depositing. Consequently, a small-scale water vapor cycling was formed partly and the upwelling and deposition of the water vapor were monitored.

4 Summary

In this study, we have presented atmospheric observations during the Tibetan Plateau atmospheric expedition experiment campaign in 2014 in Nagqu. With the help of WACAL, we observed the atmosphere in Tibetan Plateau and obtained information about the atmospheric conditions. The key findings of our study are listed below.

AMTD
8, 11925–11952, 2015

1. The calibration and validation of water vapor mixing ratio measurement have been completed. In the process of the calibration, the correlation coefficient reached up to 91.34 %. And in the process of the validation, the correlation coefficient is 93.54 % and the standard deviation is 0.77 g kg^{-1}. Considering the space and time difference between the Lidar system and radiosondes, the deviation is acceptable.

2. With WACAL, significant information about water vapor is acquired. Water vapor mixing ratio in Nagqu is measured and the case studies are provided in this paper.

3. The observations were operated in Nagqu from July to August 2014. To a certain extent, result from the abundant vegetation, precipitation, evaporation from near plateau lakes effect and the wet East Asian Monsoon and the Indian monsoon, water vapor content in Tibetan plateau during July and August was rich.

4. According to the diurnal variation of water vapor mixing ratio at 21:30 LST from July, 10 to 16 August, the trend of $W_{\mathrm{Lidar}}^{\mathrm{Cal}}$ was getting smaller with the development of the time in July and August.

5. With the help of the WACAL and the Coherent Doppler Wind Lidar, the vertical wind speed and vertical water vapor flux are calculated. The upwelling and deposition of the water vapor are monitored.

Acknowledgements. This work was partly supported by the National Natural Science Foundation of China (NSFC) under grant 41375016, 41471309 and 91337103, by the China Special Fund for Meteorological Research in the Public Interest under grant GYHY201406001. The authors wish to thank Liping Liu from CAMS/LAWS for his help and support before and during the observations. Thanks to the whole Lidar group of Ocean University of China (OUC).

References

Browell, E. V.: Remote sensing of tropospheric gases and aerosols with an airborne DIAL system, in: Optical and Laser Remote Sensing, Springer, Berlin Heidelberg, 138–147, 1983.

AMTD
8, 11925–11952, 2015

Bruneau, D., Quaglia, P., Flamant, C., Meissonnier, M., and Pelon, J.: Airborne lidar LEANDRE II for water-vapor profiling in the troposphere. I. System description, Appl. Optics, 40, 3450–3461, 2001.
Cariou, J. and Boquet, M.: LEOSPHERE Pulsed Lidar Principles, Leosphere, Orsay (France), 1–32, 2011.
Cooney, J.: Remote measurements of atmospheric water vapor profiles using the Raman component of laser backscatter, J. Appl. Meteorol., 9, 182–184, 1970.
Demtroder, W.: Molecular Physics: Theoretical Principles and Experimental Methods, Wiley VCH, Weinheim, 2005.
Dinoev, T.: Automated Raman lidar for day and night operational observation of tropospheric water vapor for meteorological applications, 2009, École Polytechnique Fédérale de Lausanne, Lausanne, 2009.
Ferrare, R., Melfi, S., Whiteman, D., Evans, K., Schmidlin, F., and Starr, D. O. C.: A comparison of water vapor measurements made by Raman lidar and radiosondes, J. Atmos. Ocean. Tech., 12, 1177–1195, 1995.
Goldsmith, J., Blair, F. H., Bisson, S. E., and Turner, D. D.: Turn-key Raman lidar for profiling atmospheric water vapor, clouds, and aerosols, Appl. Optics, 37, 4979–4990, 1998.
Grant, W. B.: Differential absorption and Raman lidar for water vapor profile measurements: a review, Opt. Eng., 30, 40–48, 1991.
Inaba, H.: Detection of atoms and molecules by Raman scattering and resonance fluorescence, in: Laser Monitoring of the Atmosphere, Springer, Berlin Heidelberg, 153–236, 1976.
Melfi, S.: Remote measurements of the atmosphere using Raman scattering, Appl. Optics, 11, 1605–1610, 1972.
Melfi, S., Lawrence Jr., J., and McCormick, M.: Observation of Raman scattering by water vapor in the atmosphere, Appl. Phys. Lett., 15, 295–297, 1969.
Papayannis, A., Ancellet, G., Pelon, J., and Megie, G.: Multiwavelength lidar for ozone measurements in the troposphere and the lower stratosphere, Appl. Optics, 29, 467–476, 1990.
Pelon, J. and Mégie, G.: Ozone monitoring in the troposphere and lower stratosphere: evaluation and operation of a ground-based lidar station, J. Geophys. Res., 87, 4947–4955, 1982.
Renaut, D. and Capitini, R.: Boundary-layer water vapor probing with a solar-blind Raman lidar: validations, meteorological observations and prospects, J. Atmos. Ocean. Tech., 5, 585–601, 1988.

AMTD
8, 11925–11952, 2015

Turner, D. D. and Goldsmith, J. E. M.: 24 h Raman lidar water vapor measurements during the Atmospheric Radiation Measurement program's 1996 and 1997 water vapor intensive observation periods, J. Atmos. Ocean. Tech., 16, 1062–1076, 1999.

Vaughan, G., Wareing, D., Thomas, L., and Mitev, V.: Humidity measurements in the free troposphere using Raman backscatter, Q. J. Roy. Meteor. Soc., 114, 1471–1484, 1988.

Wang, J., Carlson, D. J., Parsons, D. B., Hock, T. F., Lauritsen, D., Cole, H. L., Beierle, K., and Chamberlain, E.: Performance of operational radiosonde humidity sensors in direct comparison with a chilled mirror dew-point hygrometer and its climate implication, Geophys. Res. Lett., 30, 16, 2003.

Whiteman, D., Melfi, S., and Ferrare, R.: Raman lidar system for the measurement of water vapor and aerosols in the Earth's atmosphere, Appl. Optics, 31, 3068–3082, 1992.

Wulfmeyer, V. and Bösenberg, J.: Ground-based differential absorption lidar for water-vapor profiling: assessment of accuracy, resolution, and meteorological applications, Appl. Optics, 37, 3825–3844, 1998.

AMTD
8, 11925–11952, 2015

Table 1. Branches of the rotational-vibrational Raman spectrum.

$\Delta\upsilon$	ΔJ	Branch
$\pm1, \pm2$	-2	O-branch
$\pm1, \pm2$	0	Q-branch
$\pm1, \pm2$	$+2$	S-branch

AMTD
8, 11925–11952, 2015

Table 2. The shift of wave number of nitrogen and water vapor.

Molecule	Excitation wavelength	Δk	The center of the Q-branch
Nitrogen	354.7 nm	2330.7 cm^{-1}	386.7 nm
Water vapor	354.7 nm	3651 cm^{-1}	407.5 nm

AMTD
8, 11925–11952, 2015

Table 3. System specification of the Raman channel of the Lidar system.

System	Specification	
Laser	Wavelength (nm)	355
	Pulse energy (mJ)	410
	Repetition rate (Hz)	30
	Divergence (mrad)	0.5
	Pulse width (ns)	3–7
	Stability (±%)	4.0
Beam expender	Amplification factor	×10 @ 355 nm
Telescope	Aperture (mm)	304.8
	Focal length (mm)	1524
Fiber	Aperture (μm)	200
Polychromator	Collimating Lens	Focal length: 50 mm
	Grating	D: 1302 L mm^{-1} Blaze: 400 nm
	Filter-1	CWL: 407.5 ± 0.1 nm, FWHM: 0.5 ± 0.10 nm Peak %T: 50 %, OD5
	Filter-2	CWL: 386.7 ± 0.1 nm, FWHM: 0.5 ± 0.10 nm Peak %T: 50 %, OD5
	Filter-3	CWL = 354.7 nm ± 0.08 nm, FWHM: 0.5 ± 0.10 nm Peak %T: 50 %, OD5
	Lens	Focal length:100 mm
Photomultiplier tube	Photocathode Area Size (Dia. mm)	0.8
	Cathode radiant sensitivity	~ 100 mA W^{-1} @ 355 nm
	Wavelength (Peak, nm)	400
Licel	Temporal resolution (ns)	25
	Range resolution (m)	3.75
	Maximum counting rate (MHz)	250

AMTD
8, 11925–11952, 2015

Table 4. Period of time of the simultaneous observations.

May 2014	12	21	22	26	27	28	29	31
June 2014	3	4	5	6	7	8	9	10
	12	14	15	16	17	18	20	23

AMTD
8, 11925–11952, 2015

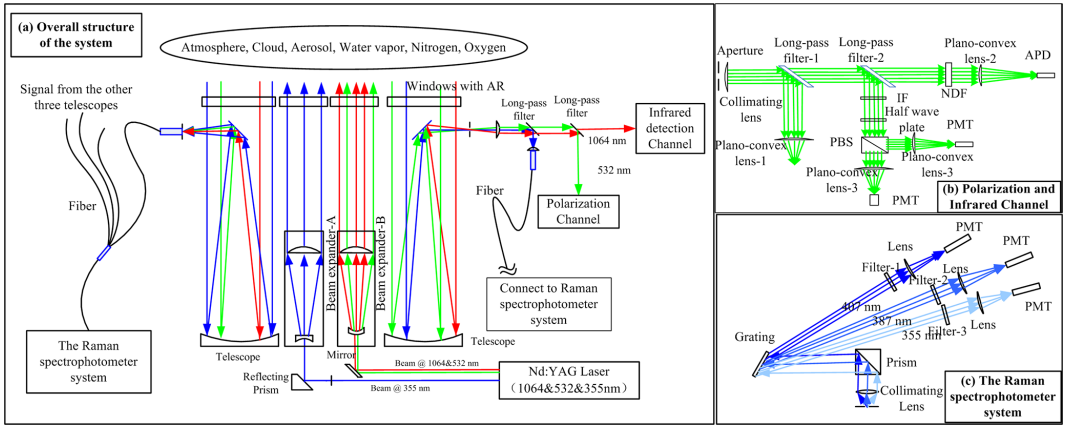

Figure 1. Schematic diagram and photos of WACAL.

AMTD
8, 11925–11952, 2015

Observations of water vapor mixing ratio and flux in Tibetan Plateau

S. Wu et al.

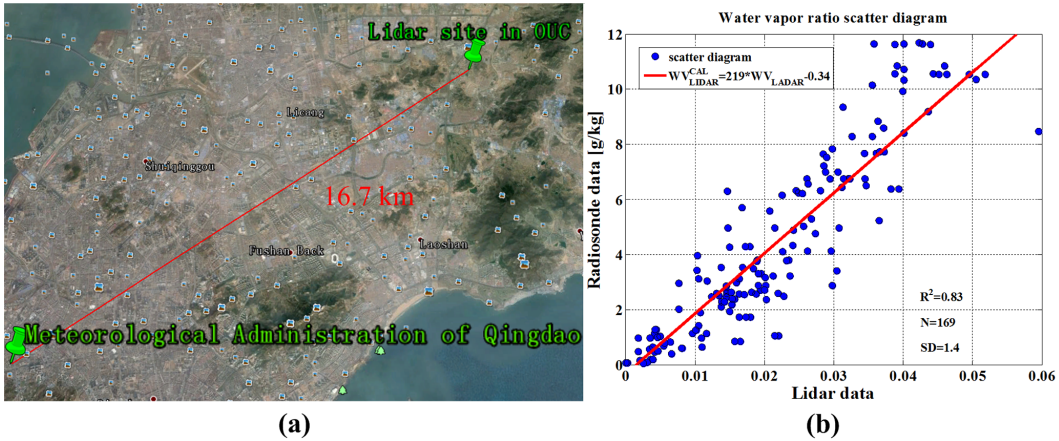

Figure 2. (a) Distance between sites of WACAL and radiosonde; **(b)** regression of WACAL mixing ratio profile to radiosonde measurement.

AMTD
8, 11925–11952, 2015

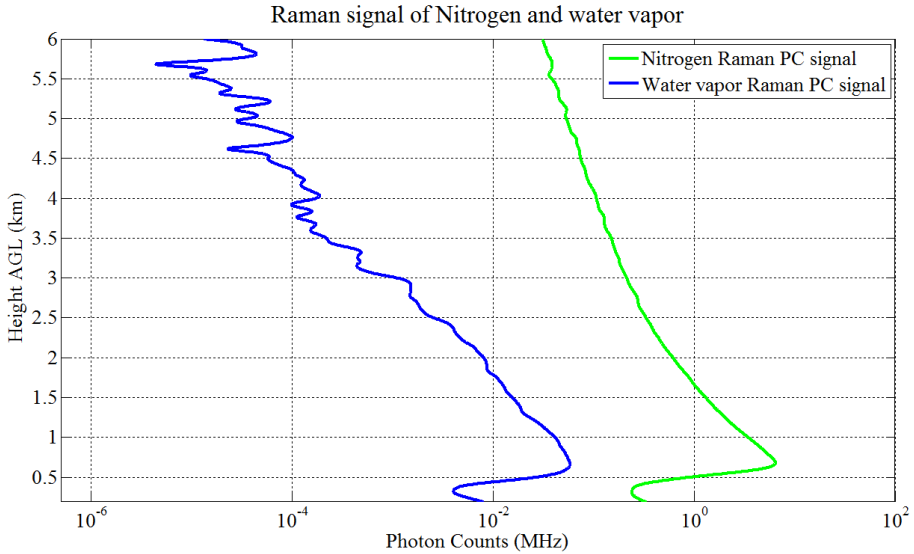

Figure 3. The actual signal detected by nitrogen and water vapor Raman channels at night time.

AMTD
8, 11925–11952, 2015

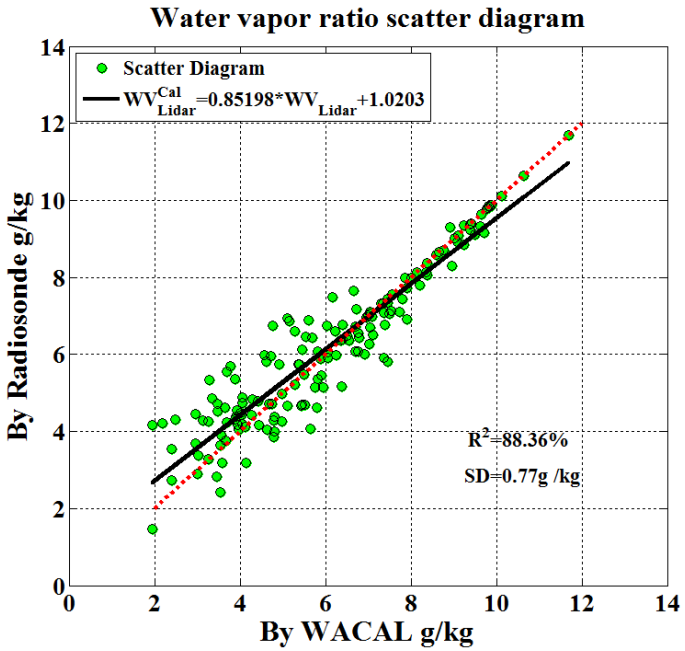

Figure 4. Validation of the calibrated water vapor mixing ratio (red dashed line is 1 : 1 curve and black line is fitting curve).

AMTD
8, 11925–11952, 2015

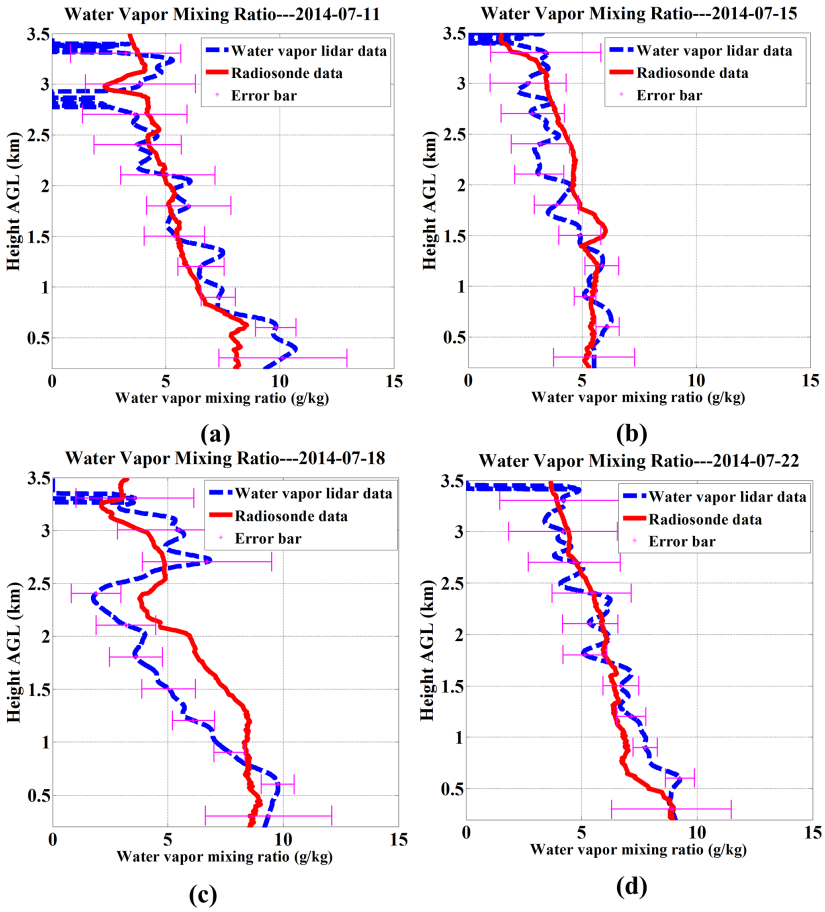

Figure 5. Water vapor mixing ratio case studies: **(a–d)** measured in Nagqu on 11, 15, 18 and 22 July 2014, respectively.

AMTD
8, 11925–11952, 2015

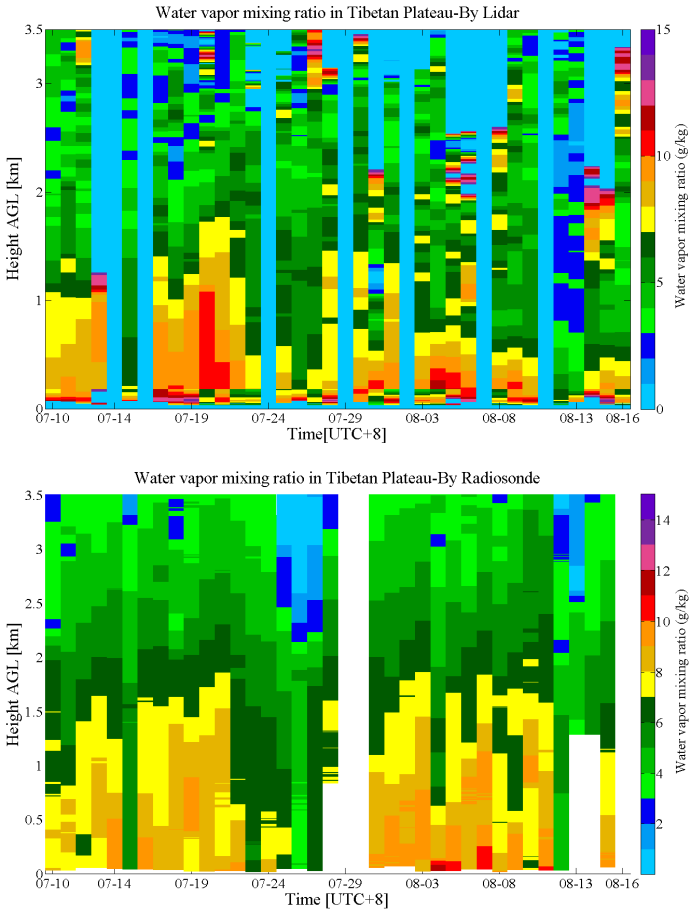

Figure 6. Diurnal variation of water vapor mixing ratio at 21:30 LST from 10 July to 16 August measured by WACAL and Radiosonde.

AMTD
8, 11925–11952, 2015

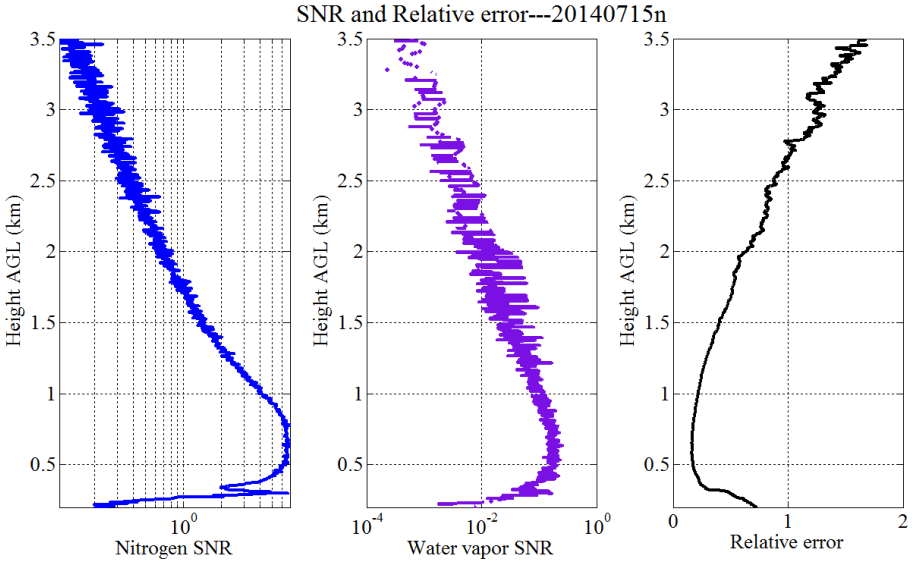

Figure 7. The SNR of nitrogen and water vapor Raman signal and the relative error of water vapor mixing ratio at night time.

AMTD
8, 11925–11952, 2015

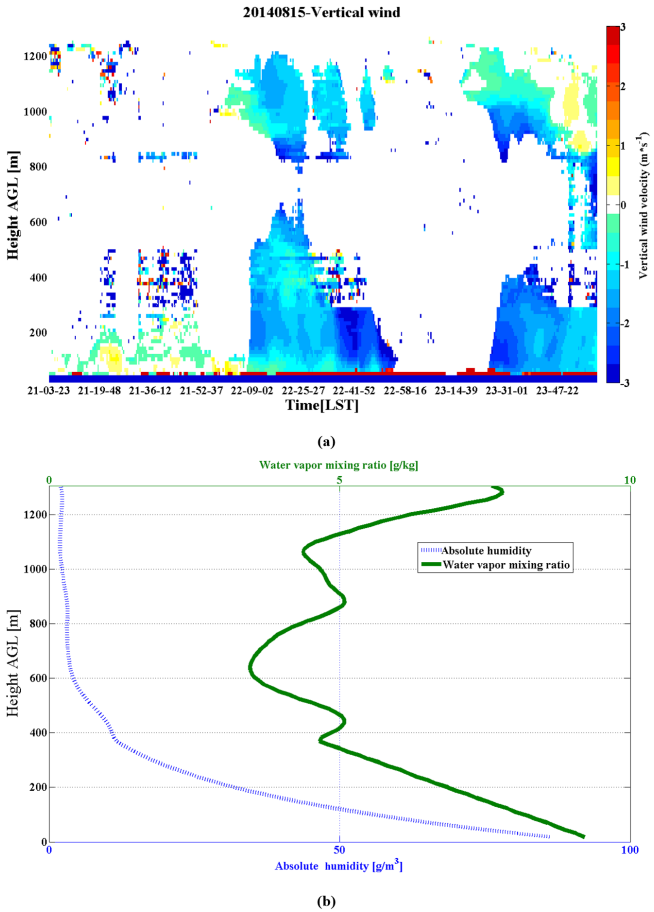

Figure 8. (a) Time serials of vertical velocity profile from 21:03 to 23:59 LST, and **(b)** profiles of water vapor mixing ratio and absolute humidity.

AMTD
8, 11925–11952, 2015

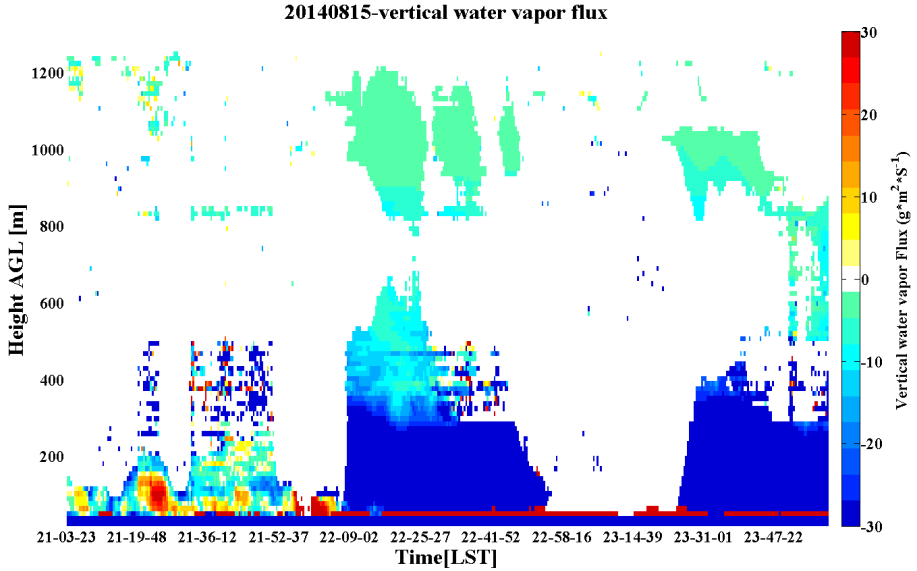

Figure 9. Time serials of vertical water vapor flux from 21:03 to 23:59 LST.

AMTD
8, 11925–11952, 2015